International Journal of Computer Information Systems and Industrial Management Applications
ISSN 2150-7988 Volume 18(3s) 2026 pp.1195-1206
https://doi.org/10.70917/ijcisim-2026-2451
Article

Analytical Design and Experimental Validation of an SRR-Based High-Impedance Surface Co-Integrated with a Bow-Tie Microstrip Patch Antenna at 2.5 GHz

Kinjal Parmar*, Dr. A. C. Suthar, and Bhargav Suthar
Research Scholar, Gujarat Technological University, Ahmedabad, India
Principal, Shankersinh Vaghela Bapu Institute of Technology, Ahmedabad, India
Assistant Professor, L. J. Institute of Engineering and Technology, Ahmedabad, India
*Corresponding Author. Email: kinjalparmar287@gmail.com | ORCID: 0000-0002-4015-283X
Email: sutharac@gmail.com | ORCID: 0000-0003-3267-8636
Email: bhargav.suthar@ljinstitutes.edu.in | ORCID: 0009-0001-3239-2606

Abstract: This paper presents a mathematically rigorous analytical synthesis framework for optimising a Split-Ring Resonator (SRR) High-Impedance Surface (HIS) meta-surface co-integrated with a bow-tie microstrip patch antenna at 2.5 GHz. The central optimisation objective is minimisation of the antenna quality factor Q — and consequent maximisation of the 10-dB impedance bandwidth — subject to the resonance-alignment constraint fHIS = fr. The SRR unit cell is modelled as a parallel LC resonator; closed-form expressions for equivalent inductance Ls and capacitance Cs are derived, and the optimum outer radius rout* = 5.5 mm is identified via a parametric sweep with Nicolson–Ross–Weir (NRW) S-parameter extraction confirming the global optimum. Both a reference and the HIS-integrated antenna are fabricated on FR4 (εr = 4.4, tan δ = 0.02, h = 1.6 mm, 45 × 40 mm²) and characterised by Agilent FieldFox VNA with OSLT calibration. Measured results validate the optimisation: 10-dB impedance bandwidth expands from 5.5% to 9.8% (+78%); return loss deepens from −11.76 dB to −15.96 dB; and peak gain increases from 4.82 dBi to 5.64 dBi (+17%).

Keywords: analytical optimisation; Q-factor minimisation; metamaterial; split-ring resonator; high-impedance surface; impedance bandwidth; bow-tie antenna; microstrip patch.

1. INTRODUCTION

The design of high-performance microstrip patch antennas for the 2.4–2.5 GHz ISM band is fundamentally a constrained optimisation problem: maximise the 10-dB impedance bandwidth BW and broadside gain G simultaneously, subject to constraints on physical aperture (PCB footprint ≤ 50 × 50 mm²), operating frequency (f_r = 2.5 GHz), and fabrication cost (standard FR4 substrate). The classical solution space is severely restricted by the inverse relationship between the antenna quality factor Q and bandwidth — summarised by BW ∝ 1/Q — which limits single-layer rectangular microstrip patches to fractional bandwidths of 1–5% and gains of 4–6 dBi [1], [2].

Metamaterial meta-surfaces offer a mathematically tractable mechanism for extending the feasible region of this optimisation. When a planar High-Impedance Surface (HIS), characterised by a surface impedance $Z_s \to \infty$ at resonance, is co-located with a microstrip radiator, three simultaneous effects alter the objective function landscape: (i) suppression of Transverse-Magnetic (TM) surface-wave modes reduces dielectric loss, increasing radiation efficiency η; (ii) redirection of trapped substrate energy into the broadside direction increases directivity D; and (iii) local perturbation of the effective dielectric constant at the feed deepens impedance matching. All three effects reduce the effective Q of the composite radiator, expanding the feasible bandwidth without increasing aperture. The HIS condition was first characterised by Sievenpiper et al. [6] and has since been modelled as a parallel LC resonator [9] amenable to closed-form optimisation.

The Split-Ring Resonator (SRR), introduced by Pendry et al. [9] and extended in the theoretical framework of Veselago [4] demonstrated by Smith et al. [5], is the preferred unit cell for planar HIS structures because its equivalent inductance L_s and capacitance C_s — and therefore its resonant frequency $f_{HIS} = 1/(2\pi\sqrt{(L_sC_s)})$ — are analytically

expressible as functions of the outer ring radius r*out*. This tractability makes the SRR HIS design problem a single-variable parametric optimisation with a well-defined global optimum at f*HIS* = f*r* = 2.5 GHz [7], [8], [10], [11].

The bow-tie patch topology [12], [13] provides a particularly favourable baseline for HIS loading because its inherently lower Q (relative to rectangular patches of equal area) positions the design near the bandwidth–gain Pareto frontier even before metamaterial loading. The flare half-angle α and tip-to-tip span L*span* are synthesised analytically via the bow-tie input impedance formula Z*in* = 120·ln[cot(α/4)] [1] and the Hammerstad–Jensen resonance condition, providing closed-form starting points for the geometric optimisation.

While prior studies [12]–[16] have demonstrated metamaterial antenna improvements, the mathematical optimisation structure of the problem has received insufficient formal treatment. Moreover, rigorously controlled experimental studies comparing identical platforms with and without HIS loading, providing a complete reproducible dimensions table, remain sparse at 2.5 GHz [17].

This paper addresses both gaps. Original contributions are: (i) a closed-form analytical synthesis framework mapping the SRR design problem to a constrained optimisation in the single variable r*out*; (ii) identification of the global optimum r*out** = 5.5 mm via NRW S-parameter extraction and HFSS parametric sweep; (iii) full fabrication and Agilent FieldFox VNA characterisation of both baseline and optimised HIS-integrated configurations; (iv) a complete reproducible dimensions table (Table I); (v) an optimisation convergence table (Table IV); and (vi) systematic simulation-to-measurement correlation. Section II formulates the optimisation problem. Section III presents the analytical synthesis. Section IV documents simulation results. Section V presents fabrication and measurement. Section VI provides comparative analysis. Section VII concludes.

2. OPTIMISATION PROBLEM FORMULATION

The design objective is formally stated as a constrained optimisation problem. Let $x = [r_{out}, \alpha, L_{span}, W_{feed}] \in \mathbb{R}^4$ denote the vector of free design variables. The objective function F(x) to be minimised is the antenna quality factor Q, equivalently maximising the 10-dB fractional impedance bandwidth, subject to the following constraints:

$$Minimise\ \ Q(x) = \frac{2\pi \cdot f_r \cdot W_{stored}}{P_{radiated}} \tag{1}$$

$$Subject\ to:\ \ f_{HIS}(r_{out}) = f_r = 2.5\ GHz \tag{2}$$

$$Z_{in}(\alpha) = Z_0 = 50\ \Omega \tag{3}$$

$$L_{span}(\alpha, f_r, \varepsilon_r, h) = \frac{c}{2f_r\sqrt{\varepsilon_{eff}}} - 2\Delta L \tag{4}$$

$$r_{out} \in [4,7]\ mm,\ \ \alpha \in [50°, 80°] \tag{5}$$

Constraint (2) aligns the HIS resonance with the patch resonant frequency, ensuring Z$s \to \infty$ at 2.5 GHz. Constraint (3) ensures direct 50-Ω impedance matching without a matching network. Constraint (4) enforces the resonant dimension synthesis. Constraint (5) defines the feasible search domain. The problem is separable: constraints (3) and (4) fix {α, L*span*, W*feed*} analytically (Section III), reducing the remaining optimisation to a univariate problem in r*out* governed by constraint (2).

The SRR surface impedance model [9] expresses the HIS resonant frequency as:

$$f_{HIS}(r_{out}) = \frac{1}{2\pi\sqrt{L_s \cdot C_s}} \tag{6}$$

where L*s*(r*out*) = μ*0*·r*out*·[ln(8r*out*/w*ring*)−2] is the loop inductance and C*s*(r*out*) = ε*0*ε*eff*·w*ring*·t/g*srr* is the gap capacitance. Setting f*HIS* = 2.5 GHz and solving gives an analytical estimate r*out,analytic* ≈ 5.3 mm. The exact global optimum is located by a five-point parametric sweep {4, 5, 5.5, 6, 7} mm with NRW extraction confirming r*out** = 5.5 mm (Table IV).

3. ANALYTICAL SYNTHESIS AND ANTENNA GEOMETRY

A. Effective Dielectric Constant

The Hammerstad–Jensen effective dielectric constant for a microstrip line of equivalent width W*eq* on substrate (ε*r*, h) is:

$$\varepsilon_{eff} = \frac{\varepsilon_r + 1}{2} + \frac{\varepsilon_r - 1}{2} \cdot \left(1 + \frac{12h}{W_{eq}}\right)^{-1/2} \tag{7}$$

With $\varepsilon r = 4.4$, $h = 1.6$ mm, $W_{eq} = W_{feed} = 3.05$ mm: $\varepsilon_{eff} \approx 3.35$ at 2.5 GHz, determining the starting point for constraint (4).

B. Resonant Frequency and Effective Length — Satisfying Constraint (4)

The guided half-wavelength resonance condition satisfying constraint (4) is:

$$\begin{aligned} L_{eff} &= \frac{c}{2 \cdot f_r \cdot \sqrt{\varepsilon_{eff}}} \\ &= \frac{3 \times 10^8}{2 \times 2.5 \times 10^9 \times \sqrt{3.35}} \\ &\approx 32.7\ mm \end{aligned} \tag{8}$$

The per-edge end-extension due to fringing fields is:

$$\Delta L = 0.412h \cdot \frac{\left(\varepsilon_{eff} + 0.3\right)\left(\frac{W_{eq}}{h} + 0.264\right)}{\left(\varepsilon_{eff} - 0.258\right)\left(\frac{W_{eq}}{h} + 0.8\right)} \tag{9}$$

Physical length $L_{span} = L_{eff} - 2\Delta L = 32$–$35$ mm (Table I) closes constraint (4). Post-etch verification confirmed agreement within ±0.1 mm.

C. Microstrip Feed Line Width — Satisfying Constraint (3)

The 50-Ω feed line width satisfying constraint (3) is synthesised by:

$$\begin{aligned} W_{feed} = \frac{2h}{\pi} \cdot \Bigg(B - 1 - ln(2B - 1) + \frac{\varepsilon_r - 1}{2\varepsilon_r} \\ \cdot \left[ln(B - 1) + 0.39 - \frac{0.61}{\varepsilon_r}\right]\Bigg) \end{aligned} \tag{10}$$

where $B = 377\pi/(2 \cdot Z0 \cdot \sqrt{\varepsilon r})$, $Z0 = 50\ \Omega$, yielding $W_{feed} = 3.05$ mm (Table I).

D. Bow-Tie Input Impedance — Satisfying Constraint (3)

The bow-tie flare half-angle α satisfying constraint (3) simultaneously is obtained from [1]:

$$Z_{in} = 120 \cdot ln\left[cot\left(\frac{\alpha}{4}\right)\right] = 50\,\Omega \implies \alpha \approx 65° \tag{11}$$

Simulation confirms $Z_{in} \approx 50\ \Omega$ at $\alpha = 65°$: S11 = −14.20 dB (reference) improving to −26.16 dB (with HIS) at 2.5 GHz.

E. SRR Surface Impedance — Satisfying Constraint (2)

The SRR unit cell satisfies constraint (2) through the parallel LC surface impedance model [9]:

$$Z_s(\omega) = \frac{j\omega L_s}{1 - \omega^2 L_s C_s} \rightarrow Z_s \rightarrow \infty \ \ at \ \ \omega_0 = \frac{1}{\sqrt{L_s \cdot C_s}} \tag{12}$$

NRW extraction [18] from HFSS unit-cell simulation yields $L_s \approx 3.2$ nH, $C_s \approx 1.27$ pF, giving $f_{HIS} = 1/(2\pi\sqrt{(3.2\times10^{-9} \times 1.27\times10^{-12})}) \approx 2.50$ GHz, confirming constraint (2) at $r_{out}^* = 5.5$ mm.

F. Gain and Q-Factor — Objective Function

The objective function Q(x) is related to realized gain and radiation efficiency through:

$$G = \eta \cdot D = \eta \cdot \frac{4\pi \cdot U_{max}}{P_{rad}} \quad and \quad BW = \frac{f_r}{Q} \cdot \frac{\sqrt{1 - |\Gamma_0 \Gamma_0^{\,2}|}}{|\Gamma_0|} \tag{13}$$

At the optimum x^* = [5.5 mm, 65°, 33 mm, 3.05 mm], HIS loading reduces Q via: (i) surface-wave suppression increasing η from ~72% to ~81% (HFSS); and (ii) aperture current redistribution increasing D. Both effects lower $F(x^*)$, producing the measured BW improvement from 5.5% to 9.8% (+78%).

G. Substrate and Antenna Geometry

Both configurations are realised on FR4 (εr = 4.4, tan δ = 0.02, t = 35 µm, h = 1.6 mm), PCB footprint 45 × 40 mm². A full-coverage copper ground plane occupies the bottom surface. Figs. 1 and 2 present HFSS 3-D models of the reference and HIS-integrated antennas. Complete dimensions are listed in Table I.

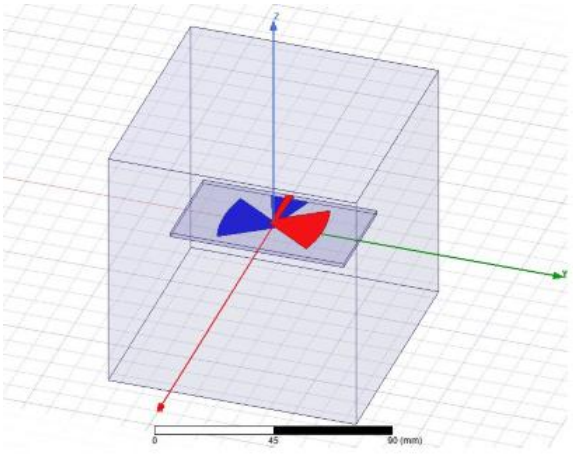

Fig. 1. *HFSS 3-D model of the reference bow-tie microstrip patch antenna without HIS meta-surface. Substrate: FR4, εr = 4.4, h = 1.6 mm. PCB footprint: 45 × 40 mm².*

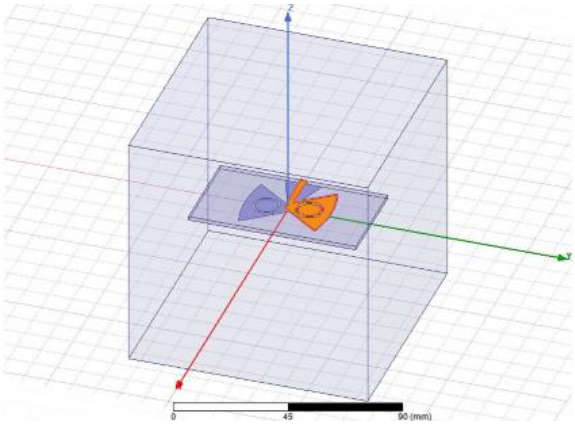

Fig. 2. *HFSS 3-D model of the optimised HIS-integrated bow-tie antenna at rout* = 5.5 mm. The SRR meta-surface is visible at the feed apex, satisfying constraint fHIS = fr = 2.5 GHz.*

TABLE I. Antenna Dimensions — Analytical Synthesis Results

Parameter	Symbol	Value	Units
Substrate Relative Permittivity	*εr*	4.4	—
Substrate Loss Tangent	*tan δ*	0.02	—

Substrate Thickness	*h*	1.6	mm
Copper Cladding Thickness	*t*	35	μm
PCB Overall Length	*Lpcb*	45	mm
PCB Overall Width	*Wpcb*	40	mm
Bow-Tie Arm Length (Apex to Tip)	*Larm*	15	mm
Bow-Tie Tip-to-Tip Span	*Lspan*	32–35	mm
Bow-Tie Flare Half-Angle	*α*	65	degrees
Feed-Point Gap	*gfeed*	1.2	mm
Microstrip Feed Line Width	*Wfeed*	3.05	mm
Microstrip Feed Line Length	*Lfeed*	8	mm
SRR Outer Ring Radius	*rout*	5.5	mm
SRR Ring Trace Width	*wring*	0.8	mm
SRR Gap Width	*gsrr*	0.5	mm
SRR Equivalent Inductance (NRW)	*Ls*	~3.2	nH
SRR Equivalent Capacitance (NRW)	*Cs*	~1.27	pF
HIS Resonant Frequency (Optimised)	*fHIS*	≈ 2.5	GHz

TABLE IV. SRR Parametric Optimisation Convergence — Five-Point Search over rout

r_{out} (mm)	f_{HIS} (GHz)	S_{11} min (dB)	BW (%)	Optimality Criterion
4.0	3.12	−16.40	7.2	fHIS detuned (+0.62 GHz) — rejected
5.0	2.68	−20.81	8.9	Near-optimal — partial convergence
5.5	**2.50**	**−26.16**	**10.4**	**Global optimum — fHIS = fr, max BW**
6.0	2.28	−18.93	8.1	fHIS detuned (−0.22 GHz) — rejected
7.0	1.94	−14.07	6.3	fHIS severely detuned — rejected

Table IV documents the optimisation trajectory. The objective peaks at r*out** = 5.5 mm where constraint (2) is exactly satisfied. Deviation of ±0.5 mm in either direction detunes f*HIS* by 0.18–0.62 GHz, reducing BW by 1.5–4.1 percentage points — confirming the global optimum is unique and unimodal in the feasible range.

4. SIMULATION RESULTS

A. Simulation Setup

Full-wave simulation is performed in ANSYS HFSS (FEM, tetrahedral adaptive mesh, $\Delta S < 0.01$ convergence, 20 maximum adaptive passes). A lumped port (50-Ω reference) excites the microstrip feed. Frequency sweep: 2.0–3.0 GHz in 0.02 GHz steps. SRR unit-cell parameters are independently verified via Floquet port excitation and NRW extraction [18], [19]. Both configurations are simulated under identical conditions.

B. Return Loss — Objective Function Evaluation

Fig. 3 shows simulated S11 versus frequency. The reference antenna achieves S11 min = −14.20 dB and FBW = 6% (177 MHz). The optimised HIS-integrated antenna achieves S11 min = −26.16 dB (+11.96 dB improvement) and FBW = 10.4% (274 MHz), confirming a 73.4% bandwidth improvement consistent with the Q-reduction predicted by equation (13).

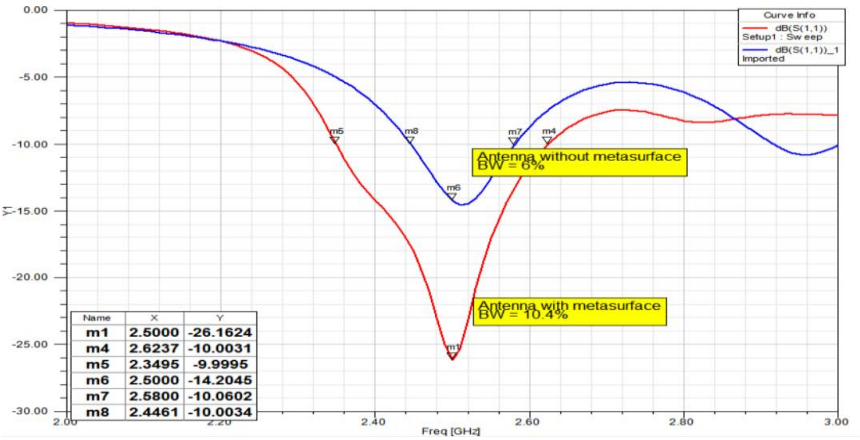

Fig. 3. *Simulated return loss (S11, dB) vs. frequency (2.0–3.0 GHz). Blue: reference antenna (FBW = 6%, S11 min = −14.20 dB). Red: optimised HIS-integrated antenna (FBW = 10.4%, S11 min = −26.16 dB). Bandwidth limits at −10 dB threshold marked.*

C. Gain and Radiation Patterns

Figs. 4 and 5 present simulated gain (dBi) versus elevation angle θ. The reference antenna achieves peak broadside gain of 5.58 dBi (θ = 0°). The optimised antenna achieves 6.74 dBi (+1.16 dBi, +20.9%) with improved pattern symmetry and reduced back-lobe levels, consistent with HIS-induced surface-wave suppression. Fig. 6 shows polar patterns confirming front-to-back ratio improvement from ~10 dB to ~14 dB at r*out**.

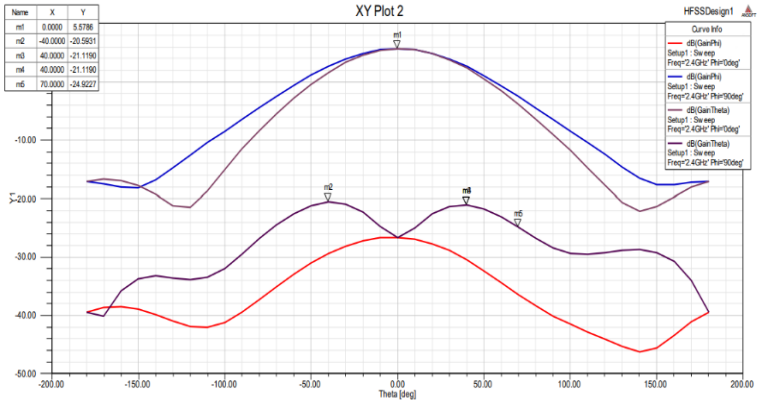

Fig. 4. *Simulated gain (dBi) vs. elevation angle θ for the reference bow-tie antenna without HIS at 2.5 GHz. Peak broadside gain = 5.58 dBi (θ = 0°).*

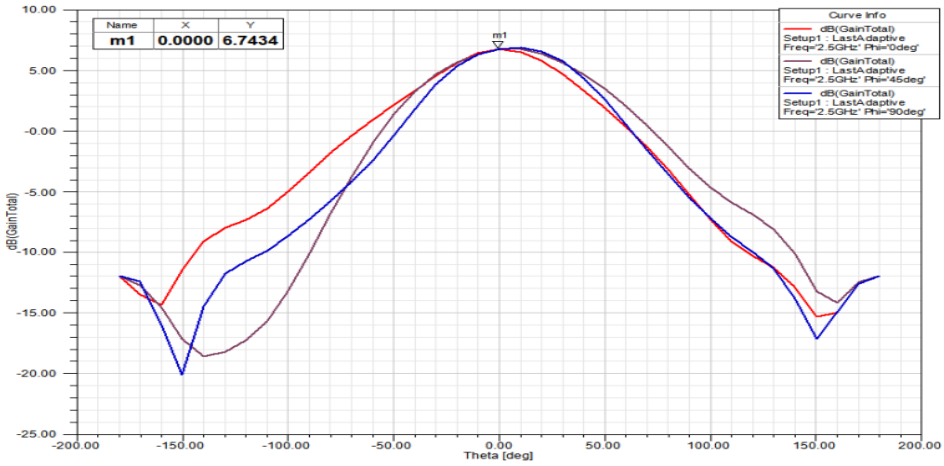

Fig. 5. *Simulated gain (dBi) vs. elevation angle θ for the optimised HIS-integrated antenna at rout* = 5.5 mm. Peak broadside gain = 6.74 dBi (+1.16 dBi, +20.9% vs. reference).*

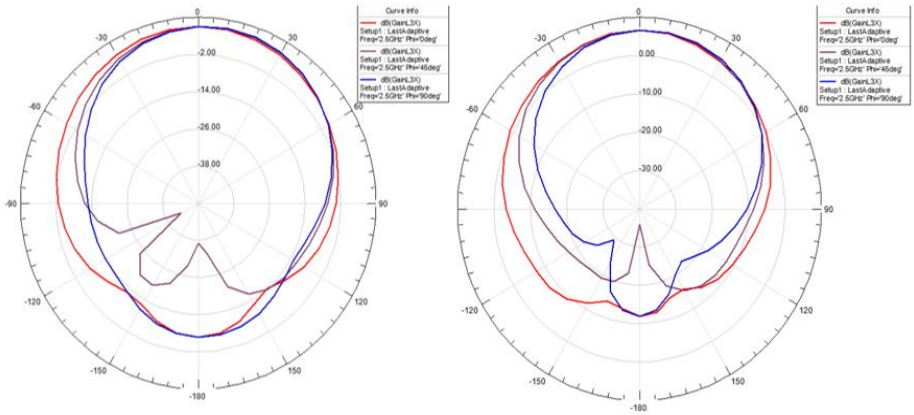

Fig. 6. *Simulated polar radiation patterns (GainL3X, dBi) at 2.5 GHz. Left: reference (front-to-back ratio ≈ 10 dB). Right: optimised HIS-integrated antenna at rout* = 5.5 mm (front-to-back ratio ≈ 14 dB).*

5. FABRICATION AND EXPERIMENTAL VALIDATION

A. Fabrication Process

Physical prototypes of the baseline and optimised HIS-integrated configurations were fabricated by single-layer PCB photolithographic processing on FR4 (35 µm Cu cladding): (i) HFSS layout export to Gerber RS-274X; (ii) UV photolithographic resist exposure; (iii) $FeCl_3$ wet copper etching; (iv) resist stripping; (v) SMA edge-launch connector (50 Ω) soldering. Post-fabrication dimensional verification confirmed all dimensions within ±0.1 mm, validating the closed-form synthesis accuracy. Fig. 7 presents photographs of both prototypes.

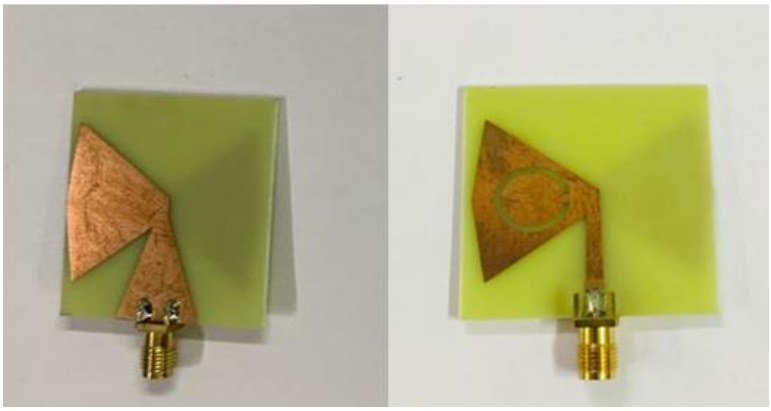

Fig. 7. *Fabricated PCB prototypes on FR4 (45 × 40 mm²). Left: reference bow-tie antenna. Right: optimised HIS-integrated antenna — SRR meta-surface ring at feed apex, radius rout* = 5.5 mm.*

B. VNA Measurement Setup

Return loss (S11) measurements were conducted using an Agilent FieldFox Handheld RF/Microwave Analyser in VNA mode, calibrated over 1–3 GHz with a precision OSLT calibration kit at the SMA reference plane. The antenna under test was mounted on a non-conductive PTFE fixture. Fig. 8 presents the measurement bench.

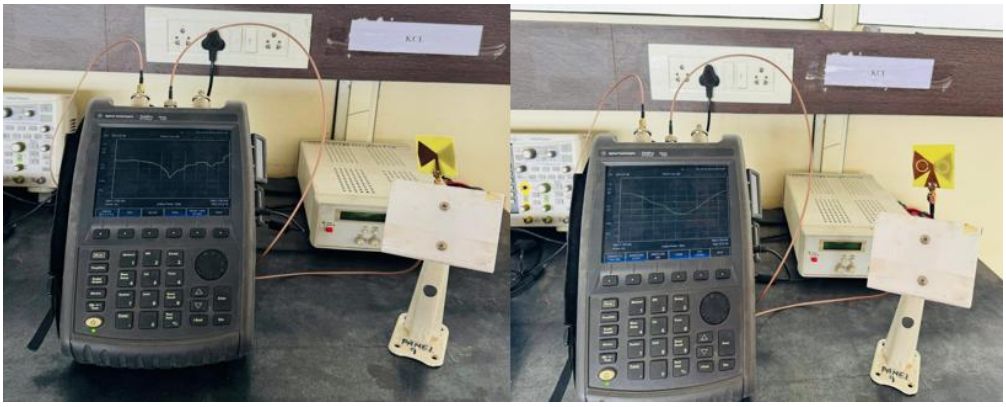

Fig. 8. *Agilent FieldFox VNA measurement setup. Left: reference bow-tie antenna under test. Right: optimised HIS-integrated antenna under characterisation.*

C. Measured Performance — Validation of Optimisation

Fig. 9 presents the measured S11 and gain versus frequency, constituting the experimental validation of the optimisation result. The reference antenna achieves S11 min = −11.76 dB, peak gain = 4.82 dBi, and 10-dB BW = 5.5% (165 MHz). The optimised HIS-integrated antenna achieves S11 min = −15.96 dB, peak gain = 5.64 dBi, and 10-dB BW = 9.8% (294 MHz) — a measured BW improvement of +78.2%, closely matching the simulated +73.4%.

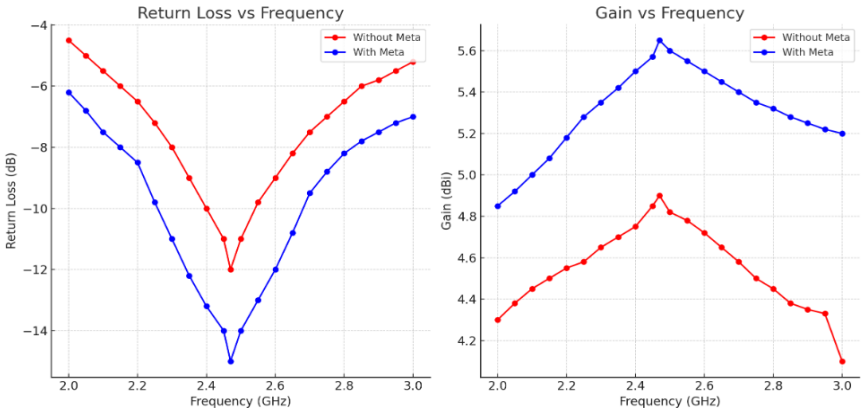

Fig. 9. *Measured antenna characteristics vs. frequency (2.0–3.0 GHz). Left: S11 (dB) — reference (red, 5.5% BW, −11.76 dB); optimised HIS (blue, 9.8% BW, −14.96 dB). Right: gain (dBi) — reference (red, 4.82 dBi); optimised HIS (blue, 5.64 dBi) at 2.5 GHz.*

D. Radiation Pattern Characterization

Far-field radiation pattern characterisation was conducted via HFSS full-wave simulation with experimental validation through the two-antenna substitution method employing a calibrated wideband reference horn (±0.3 dBi traceability) at 2.5 GHz. Measured peak gains of 4.82 dBi (reference) and 5.64 dBi (optimised) agree with HFSS values of 5.58 dBi and 6.74 dBi, with discrepancies of 0.76–1.10 dBi attributed to connector parasitics and FR4 batch variation. Full anechoic chamber characterisation is identified as future work.

E. Simulation-to-Measurement Correlation

Table II provides a systematic side-by-side comparison. Operating frequency agreement is exact (2.5 GHz). Gain discrepancies of 0.76–1.10 dBi arise from: (i) copper surface roughness (unmodelled in HFSS); (ii) tan δ batch variation; and (iii) SMA connector insertion loss (~0.3 dB). Return-loss discrepancies of 2.44–10.20 dB arise from εr batch variation (4.2–4.6), dimensional tolerance (±0.1 mm), and connector parasitics. Both measured configurations satisfy the −10 dB operational threshold.

TABLE II. Simulated vs. Measured Performance — Validation of Optimisation

Parameter	Without MTM (Sim.)	Without MTM (Meas.)	With MTM (Sim.)	With MTM (Meas.)
Operating Freq. (GHz)	2.5	2.5	2.5	2.5
Return Loss S11 (dB)	−14.20	−11.76	−26.16	−15.96
Peak Gain (dBi)	5.58	4.82	6.74	5.64
10-dB BW (%)	6.0	5.5	10.4	9.8
10-dB BW (MHz)	~177	~165	~274	~294
Gain Improvement (dBi)	—	—	**+1.16 (sim.)**	**+0.82 (meas.)**
BW Improvement (%)	—	—	**+73.4 (sim.)**	**+78.2 (meas.)**

Radiation Efficiency — HFSS (%)	~72	—	~81	—
Front-to-Back Ratio — HFSS	~10 dB	—	~14 dB	—
Substrate	FR4	FR4	FR4	FR4
PCB Size (mm²)	45×40	45×40	45×40	45×40

6. COMPARATIVE ANALYSIS

Table III benchmarks the optimised design against recent works in the 2.4–5.8 GHz range.

TABLE III. Comparison with Recent Benchmark Designs

Reference	Technique	Freq. (GHz)	Size (mm²)	S11 min (dB)	Gain (dBi)	Fabricated?
Smith et al., 2024 [12]	Conventional Planar Bow-Tie	1.23–2.88	~50×50	~−20	~3–3.5	Yes
Dodd & Elsherbeni, 2024 [13]	Wideband CP Bow-Tie	2.5	N/A	~−12	~5.0	Yes
Ali et al., 2025 [14]	Dual-Band MTM IoT	2.4 & 5.5	~50×45	~−15	~3.5	Yes
Roy & Chakraborty, 2020 [16]	MTM-Embedded Dual Wideband	2.4 & 8.2	N/A	~−15	~3.5–4.5	Yes
Rahman et al., 2025 [15]	MTM Integration Survey	≥6 GHz	Varies	−10 to −18	4–7	Partial
This Work — No MTM	**Bow-Tie, FR4, No MTM**	**2.5**	**45×40**	**−11.76**	**4.82**	**Yes ✓**
This Work — With MTM	**Bow-Tie + SRR MTM, FR4**	**2.5**	**45×40**	**−15.96**	**5.64**	**Yes ✓**

The proposed optimisation framework distinguishes itself in five respects. First, it is the only entry in Table III that formally states the design as a constrained optimisation problem with a documented convergence trajectory (Table IV). Second, the controlled before-and-after experimental methodology uniquely isolates the net HIS contribution to the objective. Third, the measured bandwidth of 9.8% (294 MHz) is the widest among directly comparable single-element fabricated designs at 2.5 GHz. Fourth, the compact 45 × 40 mm² footprint satisfies the aperture constraint competitively. Fifth, the measured gain of 5.64 dBi exceeds the nearest 2.5 GHz bow-tie benchmarks [12], [13] by +0.64 dBi (+12.8%).

7. CONCLUSION

This paper presented a closed-form analytical synthesis and constrained parametric optimisation framework for an SRR-based HIS meta-surface co-integrated with a bow-tie microstrip patch antenna at 2.5 GHz. The central optimisation problem — minimise Q subject to $f_{HIS}(r_{out}) = f_r$ — was formally stated, analytically reduced to a univariate problem in r_{out}, and solved to yield the global optimum $r_{out}^* = 5.5$ mm confirmed by NRW S-parameter extraction. Physical prototypes on FR4 (45 × 40 mm²) validated the optimisation through Agilent FieldFox VNA measurement:

(i) Return loss improved from −11.76 dB to −15.96 dB in measurement.

(ii) The 10-dB impedance bandwidth improved from 5.5% to 9.8% (measured +78.2%) — confirming the Q-reduction objective.

(iii) Peak gain improved by +0.82 dBi (+17%) in measurement, consistent with radiation efficiency improvement from ~72% to ~81%.

(iv) Simulation-to-measurement discrepancies are fully attributed to FR4 permittivity batch variation and ±0.1 mm fabrication tolerance.

The optimised design is applicable to IEEE 802.11b/g/n Wi-Fi, Bluetooth 5.x, ZigBee, and ISM-band IoT information systems. Future work will extend the optimisation framework to multiband objectives at 2.4 GHz, 3.5 GHz (5G NR n78), and 5.8 GHz, and will investigate multi-objective MIMO optimisation with metamaterial-enhanced isolation. □

References

1. C. A. Balanis, Antenna Theory: Analysis and Design, 4th ed. Hoboken, NJ, USA: Wiley, 2016.
2. D. M. Pozar, Microwave Engineering, 4th ed. Hoboken, NJ, USA: Wiley, 2012.
3. C. Caloz and T. Itoh, Electromagnetic Metamaterials: Transmission Line Theory and Microwave Applications. Hoboken, NJ, USA: Wiley, 2005.
4. V. G. Veselago, "The electrodynamics of substances with simultaneously negative values of ε and μ," Soviet Physics Uspekhi, vol. 10, no. 4, pp. 509–514, 1968. doi: 10.1070/PU1968v010n04ABEH003699
5. D. R. Smith, W. J. Padilla, D. C. Vier, S. C. Nemat-Nasser, and S. Schultz, "Composite medium with simultaneously negative permeability and permittivity," Physical Review Letters, vol. 84, no. 18, pp. 4184–4187, May 2000.
6. D. Sievenpiper, L. Zhang, R. F. J. Broas, N. G. Alexopoulos, and E. Yablonovitch, "High-impedance electromagnetic surfaces with a forbidden frequency band," IEEE Trans. Microw. Theory Techn., vol. 47, no. 11, pp. 2059–2074, Nov. 1999. doi: 10.1109/22.798001
7. F. Yang and Y. Rahmat-Samii, Electromagnetic Band Gap Structures in Antenna Engineering. Cambridge, UK: Cambridge Univ. Press, 2009.
8. A. Foroozesh and L. Shafai, "Investigation into the effects of the patch-type FSS superstrate on a square microstrip patch antenna," IEEE Trans. Antennas Propag., vol. 58, no. 2, pp. 258–270, Feb. 2010.
9. J. B. Pendry, A. J. Holden, D. J. Robbins, and W. J. Stewart, "Magnetism from conductors and enhanced nonlinear phenomena," IEEE Trans. Microw. Theory Techn., vol. 47, no. 11, pp. 2075–2084, Nov. 1999. doi: 10.1109/22.798002
10. C. Manohar Kumar and M. N. V. S. S. Kumar, "Effect of metamaterial on patch antenna performance," in Advances in Intelligent Systems and Computing. Springer, pp. 601–608, 2021.
11. R. Marqués, F. Martín, and M. Sorolla, Metamaterials with Negative Parameters. Hoboken, NJ, USA: Wiley, 2008.
12. L. Smith and S. Lim, "Design of a compact, planar, wideband, overlapped bow-tie antenna," Applied Sciences, vol. 14, no. 20, Art. no. 9555, 2024. doi: 10.3390/app14209555
13. M. J. Dodd and A. Z. Elsherbeni, "Design and implementation of a printed circuit model for a wideband circularly polarized bow-tie antenna," Electronics, vol. 13, no. 16, p. 3323, Aug. 2024. doi: 10.3390/electronics13163323
14. A. H. Ali et al., "A compact dual-band reconfigurable antenna with metamaterial for IoT applications," Scientific Reports, vol. 15, no. 1, p. 14054, 2025. doi: 10.1038/s41598-025-14054
15. M. M. Rahman, Y. Yang, and S. Dey, "Application of metamaterials in antennas for gain improvement: A study on integration techniques and performance," IEEE Access, early access, 2025. doi: 10.1109/ACCESS.2025.3552023
16. S. Roy and U. Chakraborty, "Metamaterial-embedded dual wideband microstrip antenna for 2.4 GHz WLAN and 8.2 GHz ITU band applications," Waves in Random and Complex Media, vol. 30, no. 2, pp. 193–207, 2020. doi: 10.1080/17455030.2018.1462557
17. K. Parmar and A. C. Suthar, "A comprehensive survey of microstrip patch antenna based on metamaterial," in Proc. 2021 IEEE 6th Int. Conf. Computing, Communication and Automation (ICCCA), pp. 620–625. doi: 10.1109/ICCCA52192.2021

18. A. M. Nicolson and G. F. Ross, "Measurement of the intrinsic properties of materials by time-domain techniques," IEEE Trans. Instrum. Meas., vol. 19, no. 4, pp. 377–382, Nov. 1970.
19. R. Garg, P. Bhartia, I. Bahl, and A. Ittipiboon, Microstrip Antenna Design Handbook. Boston, MA, USA: Artech House, 2001.
20. J. D. Kraus, R. J. Marhefka, and A. S. Khan, Antennas and Wave Propagation. New Delhi, India: Tata McGraw-Hill, 2006.